Available online at www.sciencedirect.com
ScienceDirect
International Journal of Heat and Mass Transfer 51 (2008) 4400–4414
International Journal of HEAT and MASS TRANSFER
www.elsevier.com/locate/ijhmt

Heat transfer from a spinning disk during semi-confined axial impingement from a rotating nozzle

Muhammad M. Rahman *, Jorge C. Lallave, Ashok Kumar

Department of Mechanical Engineering, University of South Florida, Tampa, FL 33620, USA

Received 21 May 2007; received in revised form 25 January 2008
Available online 28 May 2008

Abstract

Conjugate heat transfer from a uniformly heated spinning solid disk of finite thickness and radius during a semi-confined liquid jet impingement from a rotating nozzle is studied. The model covers the entire fluid region including the impinging jet on a flat circular disk and flow spreading out downstream under the spinning confinement plate and free surface flow after exposure to the ambient gaseous medium. The model examines how the heat transfer is affected by adding a secondary rotational flow under semi-confined jet impingement. The solution is made under steady state and laminar conditions. The study considered various plate materials such as aluminum, copper, silver, constantan and silicon. Ammonia, water, flouroinert FC-77 and MIL-7808 oil were used as working fluids. The range of parameters covered included Reynolds number (220–900), Ekman number (7.08×10^{-5}–∞), nozzle-to-target spacing ($\beta = 0.25$–1.0), disk thicknesses to nozzle diameter ratio ($b/d_n = 0.25$–1.67), Prandtl number (1.29–124.44) and solid to fluid thermal conductivity ratio (36.91–2222). It was found that a higher Reynolds number increased local heat transfer coefficient reducing the interface temperature difference over the entire disk surface. The rotational rate also increased local heat transfer coefficient under most conditions. An engineering correlation relating the Nusselt number with other dimensionless parameters was developed for the prediction of the system performance.

Keywords: Semi-confined liquid jet impingement; Rotating disk; Free surface flow; Conjugate heat transfer

1. Introduction

The applications of liquid jet impingement over a rotating surface are growing in various processes encountered in mechanical, electrical and chemical engineering. The high heat transfer rate, along with the simplicity of hardware requirements makes this cooling process an attractive option in a variety of applications. In addition, rotation is used in metal etching, rinsing operations to dissolve species, surface preparation or coating and microgravity fluid handling to generate secondary flow and therefore enhance convective heat or mass transfer. The interaction of liquid jet impingement and rotation creates a very complex and powerful flow capable of improving heat transfer processes considerably in the absence of gravity.

The heat transfer rate from a surface to an impinging jet is a complex function of many parameters. The proper understanding of the effects of these parameters such as flow rate, working fluid properties, nozzle structure and orientation, nozzle-to-target spacing, spinning rate and confinement ratio are critical to achieve a reliable cooling system design. Even though a good number of publications have considered liquid jet impingement but the simultaneous spinning of top and bottom disks during a semi-confined liquid jet impingement cooling system has not been attempted in any previous investigation. The past studies are mostly restricted to the cooling of a stationary disk by free or confined liquid jet impingement. Additionally, most of these publications deal with average heat transfer measurements rather than local distributions. A review of

* Corresponding author. Tel.: +1 813 974 5625; fax: +1 813 974 3539.
E-mail address: rahman@eng.usf.edu (M.M. Rahman).

0017-9310/$ - see front matter © 2008 Elsevier Ltd. All rights reserved.
doi:10.1016/j.ijheatmasstransfer.2008.01.023

Nomenclature

C_p	specific heat (J/kg K)
b	disk thickness (m)
d	diameter (m)
g	acceleration due to gravity (m/s^2)
Ek_1	Ekman number of impingement disk $\left(v_f/\left(4\cdot\Omega_1\cdot r_d^2\right)\right)$
Ek_2	Ekman number of confinement disk $\left(v_f/\left(4\cdot\Omega_2\cdot r_d^2\right)\right)$
h	heat transfer coefficient (W/m^2 K) $(q_{int}/(T_{int}-T_J))$
H_n	distance of the nozzle from the plate (m)
k	thermal conductivity (W/m K)
nr	number of elements in the radial direction
nz	number of elements in the axial direction
Nu	Nusselt number $(h\cdot d_n/k_f)$
Nu_{av}	average Nusselt number $(h_{av}\cdot d_n/k_f)$
p	pressure (Pa)
Pr	Prandtl number $(\mu_f\cdot Cp_f/k_f)$
q	heat flux (W/m^2)
r	radial coordinate (m)
r_d	disk radius (m)
r_p/r_d	confinement plate to disk radius ratio (confinement ratio)
Re	Reynolds number $(V_J\cdot d_n/v_f)$
T	temperature (K)
$\overline{T}_{int}$	average interface temperature (K) $\left(\frac{2}{r_d^2}\int_0^{r_d} T_{int} r\mathrm{d}r\right)$
V_J	jet velocity (m/s)
$V_{r,Z,\theta}$	velocity component in the r, z and θ-direction (m/s)
z	axial coordinate (m)

Greek symbols

β	dimensionless nozzle-to-target spacing (H_n/d_n)
δ	free surface height (m)
ε	thermal conductivity ratio (k_S/k_f)
μ	dynamic viscosity (kg/m s)
v	kinematic viscosity (m^2/s)
θ	angular coordinate (rad)
Θ	dimensionless temperature $(2\cdot k_f\cdot(T_{int}-T_J)/q_w\cdot d_n)$
ρ	density (kg/m^3)
σ	surface tension (N/m)
Ω_1	angular velocity of the impingement disk (rad/s)
Ω_2	angular velocity of the confinement disk (rad/s)

Subscripts

atm	ambient
av	average
f	fluid
int	interface
J	jet or inlet
n	nozzle
p	plate
S	solid
w	bottom surface of the impingement disk

both analytical and experimental studies on jet impinging on a flat surface has been presented by Polat et al. [1].

When a liquid jet impinges on a circular disk, the fluid spreads radially as a thin film. A boundary layer develops along the disk radius. This film is responsible for convective heat removal from the disk surface. The flow can be divided into two regions, the impingement or stagnation zone, and the wall jet region. A theoretical study of circular laminar impinging jet spreading into a thin film was done by Watson [2]. Chaudhury [3] presented the heat transfer aspect of Watson's problem. Confinement of impinging slot jet flows by a plate parallel to the impingement surface was studied by Korger and Krizek [4], Kumada and Mabuchi [5], Miyazaki and Silberman [6], Sparrow and Wong [7] and Polat et al. [8,9]. Al-Sanea [10] presented a numerical model that studied three cases: free jet, semi-confined jet and semi-confined jet impingement through a crossflow for laminar slot jet impinging on an isothermal flat surface. Moreno et al. [11] investigated the mass transfer behavior of a confined impinging jet applied to wet chemical process such as water rinsing, metal etching or platting and potential applicability of printed wiring board's fabrication. Webb and Ma [12] presented a review of studies on jet impingement heat transfer.

Morris and Garimella [13] computationally investigated the flow fields in the orifice and confinement regions of a normally impinging, axisymmetric, confined and submerged liquid jet. Garimella and Nenaydykh [14], Fitzgerald and Garimella [15], Li et al. [16], and Rahman et al. [17], all considered a confining top wall such as the one used at the present study for a submerged liquid jet. However, no rotation was used. These studies covered a number of working fluids including flouroinert (FC-77) and ammonia (NH_3) at different volumetric flow rates. Li and Garimella [18] experimentally investigated the influence of fluid thermo-physical properties on heat transfer from confined and submerged impinging jets.

Chatterjee and Deviprasath [19] numerically investigated the heat transfer to a laminar impinging jet at small nozzle-to-plate distances. Ichimiya and Yamada [20] studied the heat transfer and flow characteristics of a single circular laminar impinging jet including buoyancy effect in a narrow space with a confining wall. Temperature distribution and velocity vectors in the space were obtained numerically. Shi et al. [21] carried out numerical experiments to examine the effects of thermo-physical properties of fluid with Prandtl number range from 0.7 to 71 under a semi-confined laminar jet. Qing-Guang et al. [22] studied the

flow characteristics associated with a three-dimensional laminar impinging jet issuing from a square pipe nozzle. The authors discussed the flow field characteristics for different nozzle-to-plate spacing and Reynolds numbers. Dano et al. [23] investigated the flow and heat transfer characteristics of confined jet array impingement with crossflow.

The jet impingement on a rotating disk adds more complexity to the flow field. Carper and Deffenbaugh [24] conducted experiments to determine the average heat transfer coefficients for the rotating solid–fluid interface, with uniform temperature, cooled by a single liquid jet of oil impinging normal to the rotating disk. Carper et al. [25] conducted further experiments to consider the Prandtl number effects on the average heat transfer coefficient at the rotating disk. Thomas et al. [26] performed a one-dimensional analysis of the hydrodynamic and thermal characteristics of the boundary layers with and without rotation. The heat transfer results at the interface were greater under rotation due to a thinner thermal boundary layer. Thomas et al. [27] measured the film thickness across a stationary and rotating horizontal disk using the capacitance technique, where the liquid was delivered to the disk by a controlled semi-confined impinging jet.

Rahman and Faghri [28] presented the results of a numerical simulation of the flow field and associated heat transfer coefficient for the free surface flow of a thin liquid film adjacent to a horizontal rotating disk. Rahman and Faghri [29] analyzed the processes of heating and evaporation in a thin liquid film adjacent to a horizontal disk rotating about its vertical axis at a constant angular velocity. Faghri et al. [30] experimentally and numerically studied the heat transfer effect from a heated horizontal disk to a film of liquid from a controlled impinging jet under a partially confined condition. Heat transfer data were collected along the radius of the disk for different volumetric flow rates and inlet temperatures for supercritical and subcritical regions. Saniei et al. [31] investigated heat transfer coefficient from a rotating disk during jet impingement when the jet was placed perpendicular to the disk surface at four different distances from the center of the disk. Saniei and Yan [32] presented local heat transfer measurements for a rotating disk cooled with an impinging air jet.

The characterization of a thin film of water from an axisymmetric controlled impinging jet over a stationary and rotating disk surfaces were experimentally studied by Ozar et al. [33,34]. The authors measured the thickness of the liquid film on the disk surface by an optical method, including the characterization of the hydraulic jump. In a later study, Rice et al. [35] presented an analysis of the liquid film and heat transfer characteristics of a free surface controlled liquid jet impingement onto a rotating disk. Computations were run for a two-dimensional axisymmetric Eulerian mesh while the free surface was calculated with the volume of fluid method.

Although the above investigations provided very useful information, only a few attempted to produce local heat transfer distribution for a rotating disk in combination with a semi-confined liquid jet impingement. In addition, none of the studies have considered the rotation of the nozzle cover plate to further induce fluid motion at microgravity. The intent of this research is to study this effect with a uniform steady flow over a solid spinning disk that is partially confined with a spinning plate attached to the nozzle. Even though several approaches can be used for enhancement of heat transfer during jet impingement over a rotating disk such as triggering turbulence in the flow field by increasing the flow rate or rotational speed; the present study considered only laminar flow to address enhancement with low flow rate that is critical in space borne applications to accomplish the job with lower fluid inventory and hence lower mass of the cooling system. A higher rate of rotation is expected to enhance heat transfer at the impingement region, but may result in flow separation from the heat transfer surface further downstream which is not desirable. Therefore, the present study is quite significant in addressing the heat transfer enhancement under certain conditions. Calculations were done under five different flow rates or jet Reynolds numbers, six spinning rates or Ekman numbers, five different disk thicknesses and four nozzle-to-target spacings. A broad range of Prandtl number was covered with the use of four working fluids, namely water (H_2O), ammonia (NH_3), flouroinert (FC-77) and MIL-7808 lubricating oil. The thermal conductivity effect was studied with the implementation of five different disk materials: aluminum, Constantan, copper, silicon, and silver. The results offer a better understanding of the fluid mechanics and heat transfer behavior of semi-confined liquid jet impingement.

2. Mathematical model

A schematic of the physical problem is shown in Fig. 1. An axisymmetric liquid jet is discharged through a nozzle and impinges at the center of a solid uniformly heated circular disk. The top plate acts as an insulated partially confined spinning boundary that ends allowing the free

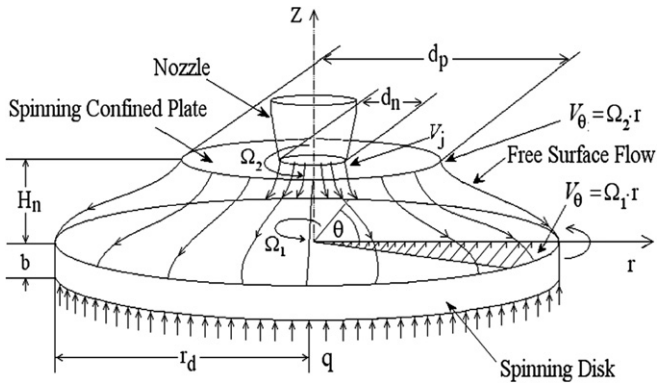

Fig. 1. Three-dimensional schematic of axisymmetric semi-confined liquid jet impingement on a uniformly heated spinning disk.

surface boundary condition exposure of the fluid. The present study considered an incompressible, Newtonian, and axisymmetric flow under a steady state condition. The variation of fluid properties with local temperature was taken into account. Due to rotational symmetry of the problem the $\partial/\partial\theta$ terms could be omitted. The equations describing the conservation of mass, momentum (r, θ and z directions, respectively), and energy can be written as [36]:

$$\frac{1}{r}\frac{\partial}{\partial r}(\rho_f r V_r)+\frac{\partial}{\partial z}(\rho_f V_Z)=0 \tag{1}$$

$$\begin{aligned}\rho_f\left(V_r\frac{\partial V_r}{\partial r}+V_Z\frac{\partial V_r}{\partial z}-\frac{V_\theta^2}{r}\right)&=-\frac{\partial p}{\partial r}+\frac{1}{r}\frac{\partial}{\partial r}\left[\frac{2}{3}\cdot\mu_f r\left(2\frac{\partial V_r}{\partial r}-\frac{V_r}{r}-\frac{\partial V_Z}{\partial z}\right)\right]\\&+\frac{\partial}{\partial z}\left[\mu_f\left(\frac{\partial V_r}{\partial z}+\frac{\partial V_Z}{\partial r}\right)\right]+\frac{2}{3}\cdot\frac{\mu_f}{r}\left(\frac{\partial V_r}{\partial r}+\frac{\partial V_Z}{\partial z}-\frac{2\cdot V_r}{r}\right)\end{aligned} \tag{2}$$

$$\begin{aligned}\rho_f\left(V_r\frac{\partial V_\theta}{\partial r}+V_Z\frac{\partial V_\theta}{\partial z}+\frac{V_r V_\theta}{r}\right)&=\frac{1}{r^2}\frac{\partial}{\partial r}\left[r^2\mu_f\left[r\frac{\partial}{\partial r}\left(\frac{V_\theta}{r}\right)\right]\right]+\frac{\partial}{\partial z}\left[\mu_f\left(\frac{\partial V_\theta}{\partial z}\right)\right]\end{aligned} \tag{3}$$

$$\begin{aligned}\rho_f\left(V_r\frac{\partial V_Z}{\partial r}+V_Z\frac{\partial V_Z}{\partial z}\right)&=-\rho_f g-\frac{\partial p}{\partial z}+\frac{1}{r}\frac{\partial}{\partial r}\left[r\mu_f\left(\frac{\partial V_r}{\partial z}+\frac{\partial V_Z}{\partial r}\right)\right]\\&+\frac{\partial}{\partial z}\left[\frac{2}{3}\mu_f\left(2\frac{\partial V_Z}{\partial z}-\frac{V_r}{r}-\frac{\partial V_r}{\partial r}\right)\right]\end{aligned} \tag{4}$$

$$\begin{aligned}\rho_f\left(V_r\frac{\partial(Cp_f T_f)}{\partial r}+V_Z\frac{\partial(Cp_f T_f)}{\partial z}\right)&=\frac{1}{r}\frac{\partial}{\partial r}\left(k_f r\frac{\partial T_f}{\partial r}\right)+\frac{\partial}{\partial z}\left(k_f\frac{\partial T_f}{\partial z}\right)+2\cdot\mu_f\left[\left(\frac{\partial V_r}{\partial r}\right)^2+\left(\frac{V_r}{r}\right)^2\right.\\&+\left(\frac{\partial V_Z}{\partial z}\right)^2+\frac{1}{2}\left(\frac{\partial V_\theta}{\partial r}-\frac{V_\theta}{r}\right)^2+\frac{1}{2}\left(\frac{\partial V_\theta}{\partial z}\right)^2\\&\left.+\frac{1}{2}\left(\frac{\partial V_r}{\partial z}+\frac{\partial V_Z}{\partial r}\right)^2-\frac{1}{3}\left(\frac{\partial V_r}{\partial r}+\frac{V_r}{r}+\frac{\partial V_Z}{\partial z}\right)^2\right]\end{aligned} \tag{5}$$

The variation of thermal conductivity of solids with temperature was not significant. Therefore, the conservation of energy inside the solid can be characterized by the following equation:

$$\frac{\partial^2 T_S}{\partial r^2}+\frac{1}{r}\left(\frac{\partial T_S}{\partial r}\right)+\frac{\partial^2 T_S}{\partial z^2}=0 \tag{6}$$

The following boundary conditions were used to complete the physical problem formulation.

$$\text{At}\quad r=0,\quad -b\leqslant z\leqslant 0:\frac{\partial T_S}{\partial r}=0 \tag{7}$$

$$\text{At}\quad r=0,\quad 0\leqslant z\leqslant H_n: V_\theta=V_r=0,\quad \frac{\partial V_Z}{\partial r}=0,\quad \frac{\partial T_f}{\partial r}=0 \tag{8}$$

$$\text{At}\quad r=r_d,\quad -b\leqslant z\leqslant 0:\frac{\partial T_S}{\partial r}=0 \tag{9}$$

$$\text{At}\quad r=r_d,\quad 0\leqslant z\leqslant \delta: p=p_{atm} \tag{10}$$

$$\text{At}\quad z=-b,\quad 0\leqslant r\leqslant r_d:-k_S\frac{\partial T_S}{\partial z}=q \tag{11}$$

$$\text{At}\quad z=0,\quad 0\leqslant r\leqslant r_d: V_r=V_Z=0,\quad V_\theta=\Omega_1\cdot r,\quad T_f=T_S,\quad k_S\frac{\partial T_S}{\partial z}=k_f\frac{\partial T_f}{\partial z} \tag{12}$$

$$\text{At}\quad z=H_n,\quad 0\leqslant r\leqslant \frac{d_n}{2}: V_Z=-V_J,\quad V_r=V_\theta=0,\quad T_f=T_J \tag{13}$$

$$\text{At}\quad z=H_n,\quad \frac{d_n}{2}\leqslant r\leqslant r_p: V_r=V_Z=0,\quad V_\theta=\Omega_2\cdot r,\frac{\partial T_f}{\partial z}=0 \tag{14}$$

The boundary condition at the free surface can be expressed as

$$\text{At}\quad z=\delta,\quad r_p\leqslant r\leqslant r_d:\frac{\partial\delta}{\partial r}=\frac{V_Z}{V_r},\quad p=p_{atm}-\frac{\sigma\frac{d^2\delta}{dr^2}}{\left[1+\left(\frac{d\delta}{dr}\right)^2\right]^{3/2}},\quad \frac{\partial V_S}{\partial n}=0,\quad \frac{\partial T_f}{\partial n}=0 \tag{15}$$

where V_S is the fluid velocity component along the free surface and n is the coordinate normal to the free surface. The local and average heat transfer coefficients can be defined as

$$h=\frac{q_{int}}{T_{int}-T_J} \tag{16}$$

$$h_{av}=\frac{2}{r_d^2\cdot(\overline{T}_{int}-T_J)}\int_0^{r_d} hr(T_{int}-T_J)dr \tag{17}$$

where $\overline{T}_{int}$ is the average temperature at the solid–liquid interface. The local and average Nusselt numbers are calculated according to the following expressions:

$$Nu=\frac{h\cdot d_n}{k_f} \tag{18}$$

$$Nu_{av}=\frac{h_{av}\cdot d_n}{k_f} \tag{19}$$

The characteristics of the flow are controlled by three major physical parameters: the Reynolds number, $Re_J=V_J d_n/\nu_f$, the dimensionless nozzle-to-target spacing ratio, $\beta=H_n/d_n$, and the Ekman number, $Ek_{1,2}=\nu_f/4\Omega_{1,2}r_d^2$. The values of Reynolds number was limited to a maximum of 900 to stay within the laminar region. The nozzle opening and the heated target disk have a radius of 0.6 and 6.0 mm, respectively. The heat flux (q) was kept constant at 125 kW/m^2. The incoming fluid jet temperature (T_J)

was 310 K for water and FC-77, 303 K for ammonia (at a pressure of 20 bars), and 373 K for MIL-7808. The thickness of the disk was varied over the following values: 0.3, 0.6, 1.0, 1.5, and 2.0 mm. The jet impingement height or the distance between the nozzle and disk was set at the following values: 3×10^{-4}, 6×10^{-4}, 9.0×10^{-4}, and 1.2×10^{-3} m. The spinning rate (Ω) was varied from 0 to 78.54 rad/s or 0 to 750 rpm. The flow rate was varied from 6.65×10^{-7} to 2.72×10^{-6} m^3/s. The range for Reynolds number and Ekman number were: $Re = 220$–900 and $Ek_{1,2} = 7.08 \times 10^{-5}$ to ∞. The possibility of getting into turbulent flow due to disk rotation was checked. Using the laminar–turbulent transition criterion used by Popiel and Boguslawski [37] and Vanyo [38], all runs used in the paper checked out to be laminar.

The properties of solid materials such as density, viscosity, thermal conductivity, and specific heat were obtained from Özisik [39] and assumed to remain constant over the working temperature range. Fluid properties for H_2O, NH_3, MIL–7808, and FC–77 were obtained from Bejan [40] and Bula [41]. The properties of the above fluids were correlated according to the following equations. For water between 300 K $< T <$ 411 K; $Cp_f = 9.5 \times 10^{-3}T^2 - 5.9299T + 5098.1$; $k_f = -7.0 \times 10^{-6}T^2 + 5.8 \times 10^{-3}T - 0.4765$; $\rho_f = -2.7 \times 10^{-3}T^2 + 1.3104T + 848.07$; and $\ln(\mu_f) = -3.27017 - 0.0131T$. For ammonia between 273.15 K $< T <$ 370 K; $Cp_f = 0.083T^2 - 40.489T + 9468$; $k_f = 1.159 - 2.30 \times 10^{-3}T$; $\rho_f = 579.81 + 1.6858T - 0.0054T^2$; and $\ln(\mu_f) = -5.33914 - 0.0115T$. For MIL-7808 between 303 K $< T <$ 470 K; $Cp_f = 903.8 + 3.332T$; $k_f = 0.18 - 1 \times 10^{-4}T$; $\rho_f = 1181 - 0.708T$; and $\ln(\mu_f) = 3.2436 - 0.0229T$. For FC-77 between 273 K $< T <$ 380 K; $Cp_f = 589.2 + 1.554T$; $k_f = 0.0869 - 8 \times 10^{-5}T$; $\rho_f = 2{,}507.2 - 2.45T$; and $\ln(\mu_f) = -2.38271 - 0.0145T$. In these correlations, the absolute temperature T is in K.

3. Numerical computation

The governing equation (1)–(6) along with the boundary conditions (7–15) were solved using the Galerkin finite element method [42]. The purpose of a finite element method is to break down the continuum problem, of essentially an infinite number of degrees of freedom, to a finite number of degrees by discrete sizing the continuum into a number of simple shaped elements. Four node quadrilateral elements were used. In each element, the velocity, pressure and temperature fields were approximated which led to a set of equations that defined the continuum. The number of elements required for accurate results was determined from a grid independence study. The size of the elements near the solid–fluid interface was made smaller to adequately capture large variations in velocity and temperature in that region.

Due to non-linear nature of the governing differential equations the Newton–Raphson method was used to arrive at the solution for the velocity and temperature fields. The approach used to solve the location of the free surface was to introduce a new degree of freedom representing the position of the free surface. This degree of freedom was introduced as a new unknown into the global system of equations. Since the solution of the momentum equation required only two out of the three boundary conditions at the free surface, the third condition was used to upgrade the position of the free surface at the end of each iteration step. The Newton–Raphson solver used spines to track the free surface and re-arranged grid distribution with the movement of the free surface. These spines are straight lines passing through the free surface nodes and connecting the nodes underneath the free surface. The free surface movement affected only nodes along the spine. The solution was considered converged when relative change in field

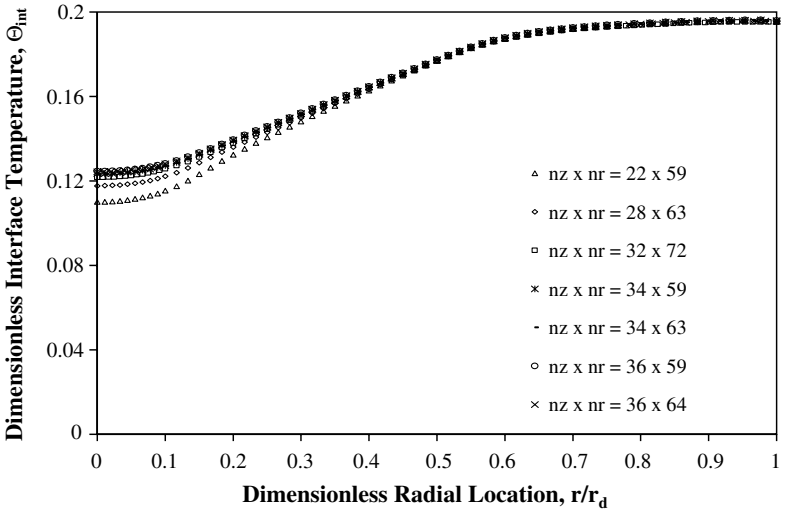

Fig. 2. Dimensionless interface temperature distributions for different number of elements in r and z directions ($Re = 750$, $b/d_n = 0.5$, $Ek_{1,2} = 4.25 \times 10^{-4}$, $r_p/r_d = 0.667$, $\beta = 0.5$).

values from a particular iteration to the next, and the sums of the residuals for each variable became less than 10^{-6}. Several grids or combinations of number of elements were used to determine the accuracy of the numerical solution as shown in Fig. 2. The numerical solution becomes grid independent when the number of divisions equal to 34×63 in the axial (z) and radial (r) directions, respectively is used. Comparing the numerical results for the 34×59 and 36×64 grids with a 34×63 grid showed an average difference of 0.159%.

4. Results and discussion

Fig. 3 presents the free surface height distribution for different plate to disk confinement ratios when the jet strikes the center of the disk while it is spinning at a rate of 125 rpm. The nozzle along with the confinement disk is also rotating at the same speed, in the same direction resulting in $Ek_{1,2} = 4.25 \times 10^{-4}$. It can be seen that the fluid spreads out radially as a wavy thin film. The film thickness decreases as the plate to disk confinement ratio decreases under the same spinning rate and flow rate. This behavior occurs due to dominance of surface tension and gravitational forces that form the free surface as the fluid leaves the confinement zone and moves downstream. When r_p is increased, the frictional resistance from both walls slows down the momentum and results in higher film thickness. For the conditions considered in the present investigation, a sudden drop in fluid height occurs for $r_p/r_d < 0.333$ because the equilibrium film height for free surface motion is significantly lower than confinement height. In this situation, liquid may not cover all the way to the end of the confinement disk and free surface may start to form within the confinement region to provide a smooth streamline for the free surface. At $r_p/r_d \geqslant 0.5$, the confinement region is fully covered with fluid and a smooth transition is seen in film height distribution after exit.

Fig. 4a shows the variation of the dimensionless interface temperature and the local Nusselt number distributions for different Reynolds numbers under a rotational rate of 275 rpm ($Ek_{1,2} = 1.93 \times 10^{-4}$). The plots in Fig. 4a reveal that dimensionless interface temperature decreases with jet velocity (or Reynolds number). At any Reynolds number, the dimensionless interface temperature has the lowest value at the stagnation point (underneath the center of the axial opening) and increases radially downstream reaching the highest value at the end of the disk. At a Reynolds number of 220, the temperature becomes practically uniform after $r/r_d > 0.667$. The thickness of the thermal boundary layer increases with radius and causes the interface temperature to increase. The increment of the dimensionless interface temperature up to the end of its confinement coincides with the thickening of the thermal boundary layer. Afterward it becomes more uniform beneath the free surface. As noted in Fig. 3, there is a significant re-adjustment of fluid layer thickness as the flow comes out of the confinement and moves downstream with a free surface at the top. Fig. 4a shows how the local Nusselt number distributions increases over a small distance (core region) measured from the stagnation point, reaching a maximum around $r/r_d = 0.05$, and then decreases along the radial distance as the boundary layer develops further downstream up to the end of the confined spinning plate or $r_p/r_d \approx 0.667$. After this location, the Nusselt number increases downstream and reaches a uniform value at larger radial locations of the disk. The location of the maximum Nusselt number can be associated with the transition of the flow from the vertical impingement to horizontal displacement where the boundary layer starts to develop. The increase of Nusselt number after the exit from the confinement is a result of significant decrease

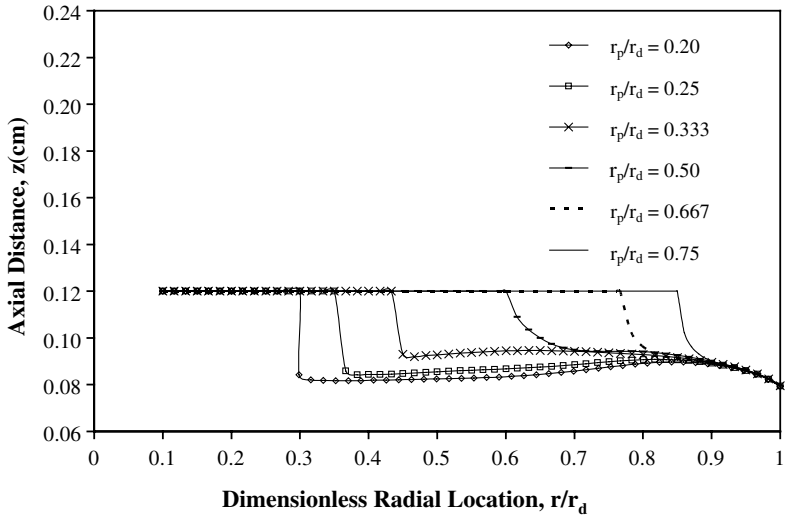

Fig. 3. Free surface height distribution for different plate to disk confinement ratio with water as the cooling fluid ($Re = 450$, $Ek_{1,2} = 4.25 \times 10^{-4}$, $\beta = 0.5$, $b/d_n = 0.5$).

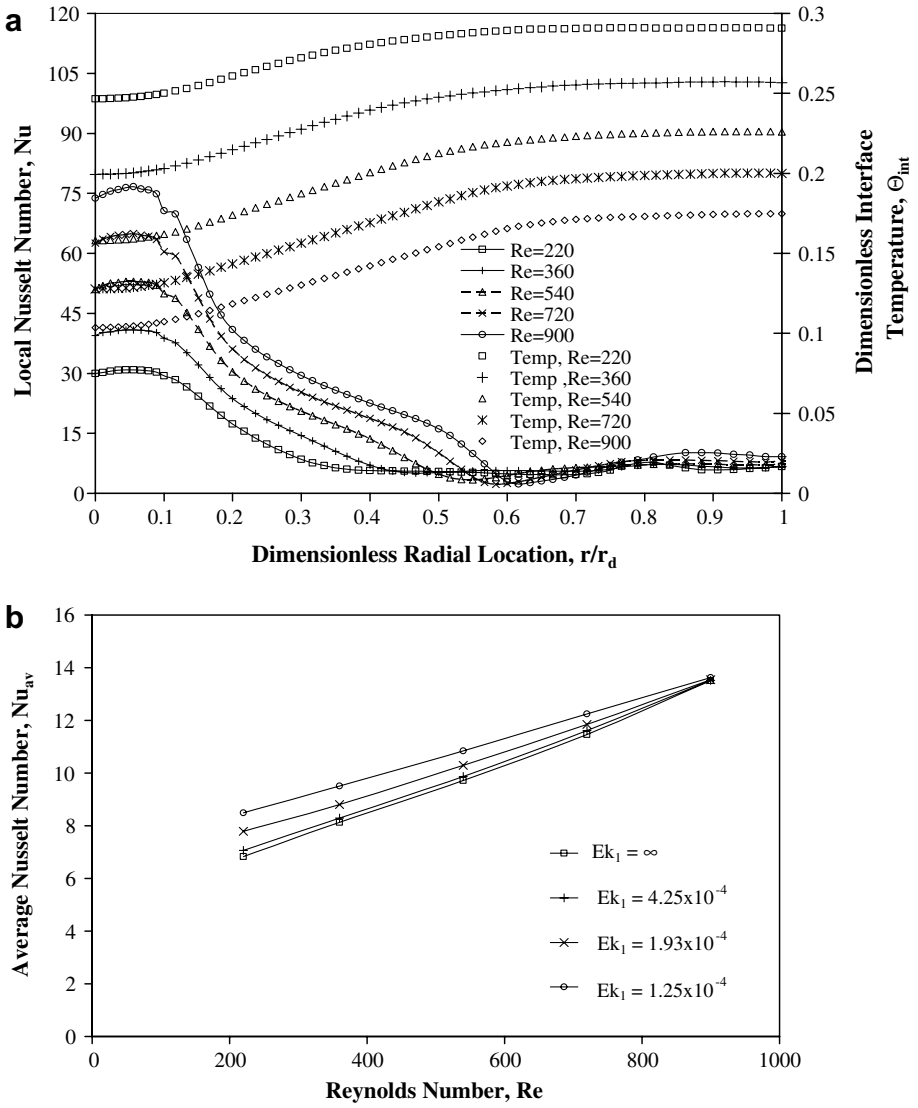

Fig. 4. Effects of Reynolds number variation for a silicon disk with water as the cooling fluid ($\beta = 0.5$, $b/d_n = 0.5$, $r_p/r_d = 0.667$). (a) Local Nusselt number and dimensionless solid–fluid interface temperature ($Ek_{1,2} = 1.93 \times 10^{-4}$). (b) Average Nusselt number at different Ekman numbers ($Ek_2 = 4.25 \times 10^{-4}$).

of film thickness that also decreases the thickness of the thermal boundary layer until it reaches a new equilibrium. It may be noticed that at low values of Reynolds number ($Re = 220$ in particular), local Nusselt number remains almost constant over a good portion of the disk including a portion within the confinement region. This is because at low Reynolds number, the jet momentum dies down and the flow is driven by rotational motion of the disks. Fig. 4a confirms to us how an increasing Reynolds number contributes to a more effective cooling. The observations are in-line with the previous studies by Garimella and Nenaydykh [14] and Saniei et al. [32].

Fig. 4b plots the average Nusselt number as a function of Reynolds number for low, intermediate, and high Ekman numbers of the solid disk. The spinning of the confined plate was done at a constant rate of 125 rpm or $Ek_2 = 4.25 \times 10^{-4}$. It may be noted that average Nusselt number increases with Reynolds number. As the flow rate (or Reynolds number) increases, the magnitude of fluid velocity near the solid–fluid interface that controls the convective heat transfer rate increases. Furthermore, at a particular Reynolds number, the Nusselt number gradually increases with the increment of disk spinning rate. This behavior confirms the positive influence of the rotational rate of the solid disk on the average Nusselt number down to $Ek_1 = 1.25 \times 10^{-4}$ that corresponds to a spinning rate of 425 rpm. It may be also noticed that the average Nusselt number plots gets closer to each other as the Reynolds number increases indicating that curves will intersect at higher Reynolds numbers. These intersections indicate the presence of a liquid jet momentum dominated region at higher Reynolds numbers. From the numerical results it was observed that the heat transfer is dominated by impingement when $Re \cdot Ek_1 > 0.113$ and dominated by disk rotation when $Re \cdot Ek_1 < 0.09$. In between there limits, both of these effects play an important role in determining

the variation of average Nusselt number. This type of behavior is consistent with the experimental results of Brodersen et al. [43] where the ratio of jet and rotational Reynolds numbers was used to characterize the flow regime.

The rotational rate effects of the solid disk under the influence of a constant spinning rate of the confinement plate on the local Nusselt number and dimensionless interface temperature are illustrated in Fig. 5a for a Reynolds number of 540 and dimensionless nozzle-to-target spacing (β) equal to 0.5. It may be noted that the local Nusselt number remains the same over the distance $0 < r/r_d < 0.35$ and increases with rotational rate (decreases with Ekman number) further downstream. This is because the flow is highly dominated by jet inlet momentum at $r/r_d < 0.35$, and the centrifugal forces generated by rotation of the disks can influence the transport only at $r/r_d > 0.35$. It may also be noted that a higher rotational rate provides a lesser amount of undershoot in Nusselt number and a higher equilibrium value at large disk radii. Fig. 5a shows that dimensionless interface temperature decreases with the increment of the rotational rate in comparison with the stationary case due to the enhancement of local fluid velocity adjacent to the disk. The local Nusselt number increases by an average of 33.78% in Fig. 5a; as the Ekman number of solid spinning disk decreases from ∞ to 7.08×10^{-5} under the influence of a constant spinning rate of 125 rpm ($Ek_2 = 4.25 \times 10^{-4}$) of the top confinement disk. The dimensionless interface temperature decreases by an average of 10.85% in Fig. 5a under a Reynolds number of 540. The enhancement of Nusselt number due to rota-

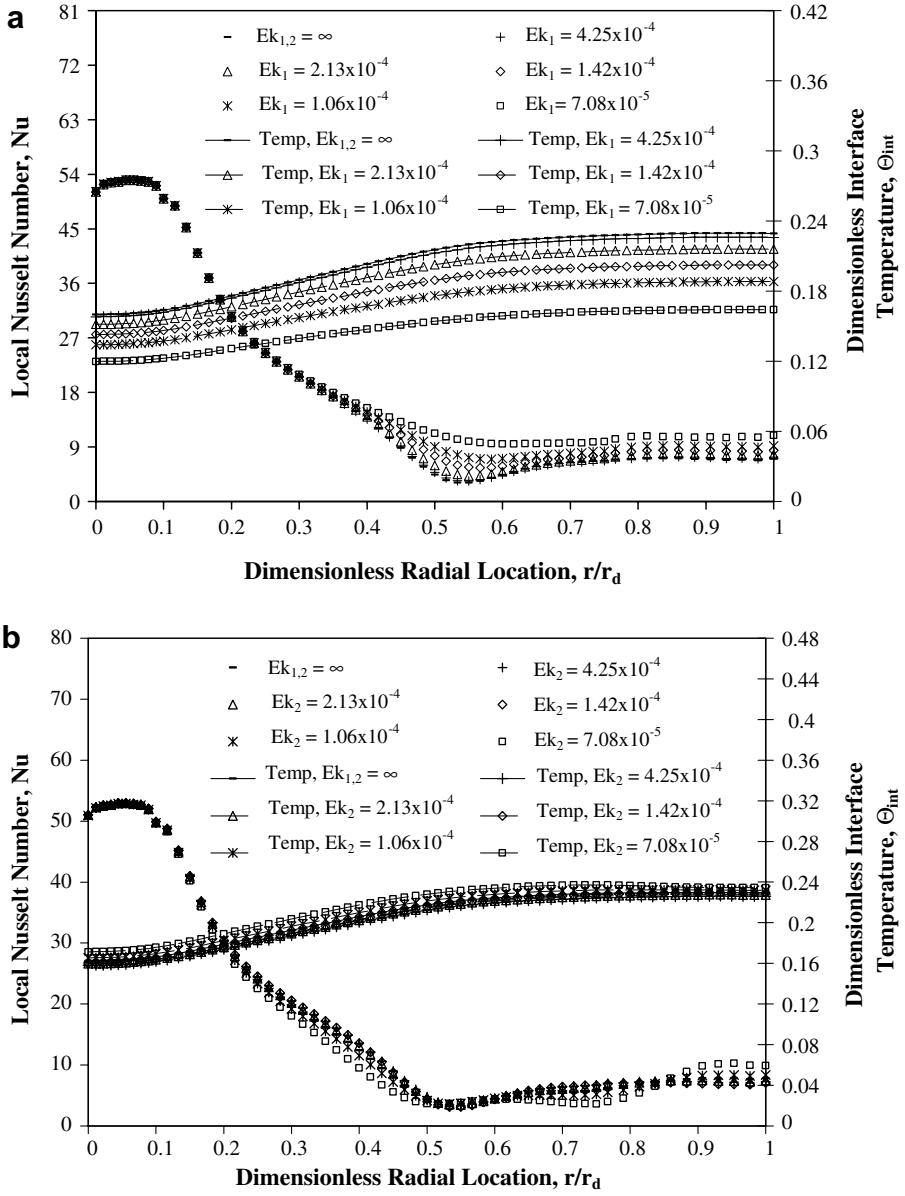

Fig. 5. Local Nusselt number and dimensionless interface temperature distributions for a silicon disk with water as the cooling fluid ($Re = 540$, $\beta = 0.5$, $b/d_n = 0.5$, $r_p/r_d = 0.667$). (a) Effects of Ek_1 variation ($Ek_2 = 4.25 \times 10^{-4}$) and (b) effects of Ek_2 variation ($Ek_1 = 4.25 \times 10^{-4}$).

tion is primarily caused by enhancement of local fluid velocity adjacent to the rotating disk surface. The tangential velocity due to rotation combined with axial and radial velocities due to jet momentum increases the magnitude of the velocity vector.

Fig. 5b shows the rotational rate effects of the top confinement disk in conjunction with a constant spinning rate of the solid impingement disk on local Nusselt number and dimensionless interface temperature distributions for a Reynolds number of 540 and dimensionless nozzle-to-target spacing (β) equal to 0.5. It may be noted that rotational effect up to a spinning rate of 375 rpm or ($Ek_2 = 1.42 \times 10^{-4}$) increases the local Nusselt number and generates lower temperature over the entire solid–fluid interface with less intensity in comparison with the Reynolds number effect shown in Fig. 4a and the solid disk rotational rate effect under a constant spinning of the confinement plate shown in Fig. 5a. Fig. 5b shows that dimensionless interface temperature decreases with the increment of the rotational rate up to a spinning rate of 375 rpm ($Ek_2 = 1.42 \times 10^{-4}$) in comparison with the stationary case due to the enhancement of local fluid velocity adjacent to the disk. The local Nusselt number increases by an average of 5.92% and the dimensionless interface temperature decreases by an average of 0.4% in Fig. 5b; as the Ekman number of the top confined plate decreases from ∞ to 1.42×10^{-4} under the influence of a constant spinning rate of 125 rpm ($Ek_1 = 4.25 \times 10^{-4}$) of the solid impingement disk. However, exceptions occur for spinning rates of 500 and 750 rpm ($Ek_2 = 1.06 \times 10^{-4}$ and 7.08×10^{-5}) where higher values for dimensionless interface temperature and lower values for Nusselt number are found for the most part of the solid–fluid interface. In these particular cases, the rotation generates a negative effect within the confined region. At these high rotational rates of the top disk (4 and 6 times compared to the bottom disk) the thermal boundary layer structure at the heated bottom disk tends to get swept away by the strong rotational motion of the top disk. Therefore a lower Nusselt number is achieved compared to other cases in the confined region. However, when the flow gets out of the confinement at ($r/r_d = 0.667$), the added momentum exerted by the top disk results in rise of heat transfer coefficient from this point all the way to the end of the disk. Therefore, the proper selection of two spinning rates is crucial in a design process. This type of behavior is consistent with the observations of Popiel and Boguslawski [37].

The effects of disk thickness variation on the dimensionless interface temperature and local Nusselt number are shown in Fig. 6a. In these plots, silicon has been used as the disk material and water as the cooling fluid for Reynolds number of 450 and spinning rate of 125 rpm ($Ek_{1,2} = 4.25 \times 10^{-4}$). The dimensionless interface temperature increases from the impingement region all the way to the end of the disk. It may be noted that the disk thickness variation curves from the 0.25 to 1.67 intersect with each other at a dimensionless radial distance of $r/r_d = 0.55$. The thicker disks generate more uniform dimensionless interface temperature due to a larger radial conduction within the disk. Since the flow rate and heat input at the bottom of the disk are kept constant, the global energy balance dictates that average interface temperature changes only slightly as the thermal resistance offered by the disk changes with the variation of disk thickness. It may be observed from Fig. 6a that average interface temperature slightly increases with the increment of disk thickness. The local distribution of interface temperature is primarily controlled by the re-distribution of input heat within the solid. A thinner plate offers a smaller opportunity for heat flux re-distribution and therefore a larger variation controlled by convection and local fluid temperature is seen. For a thicker plate, more opportunity for radial conduction results in higher interface heat flux in the impingement region where the fluid is cooler and gradually smaller interface heat flux as the fluid moves downstream. This results in more uniform interface temperature as shown in Fig. 6a. The combined effects of only slight change in average interface temperature whereas large change in local distribution with the variation of thickness results in plots intersecting each other in Fig. 6a. Local Nusselt number plots in Fig. 6a change slightly with the variation of disk thickness. In all cases, it is evident that the Nusselt number is sensitive to the solid thickness especially at the core region where higher Nusselt number values are obtained. It may be noted that local Nusselt number was calculated by using local temperature and local heat flux at the interface, both of which became larger in the impingement region with increase of disk thickness. Therefore the net effect was almost same Nusselt number distribution for all the thicknesses. This phenomenon has also been documented by Lachefski et al. [44] for jet impingement on a stationary disk.

Four different nozzle-to-target spacing ratio (β) from 0.25 to 1 were modeled using water as the coolant and silicon as the disk material. The effects of nozzle-to-target spacing on local Nusselt number and dimensionless interface temperature at a spinning rate of 125 rpm ($Ek_{1,2} = 4.25 \times 10^{-4}$) and Reynolds number of 900 are shown in Fig. 6b. It may be noticed that the impingement height quite significantly affects the Nusselt number distribution particularly at the stagnation region. A higher local Nusselt number at the core region is obtained when the nozzle is brought very close to the heated disk ($\beta = 0.25$). A lower distance between nozzle and impingement plate provides lower loss of momentum as the jet travels for a shorter distance through the surrounding liquid medium. In addition, a smaller gap provides quicker propagation of centrifugal force from the spinning disks into the fluid medium increasing the net transport rate. It may be also noticed that in Fig. 6b, curves for $\beta = 0.25$–0.75 are close together whereas, at $\beta = 1$, a higher temperature is obtained all along the disk. In Fig. 6b, it can be noticed that minimum in Nusselt number moves downstream with increase in gap and no minimum is observed at $\beta = 1$.

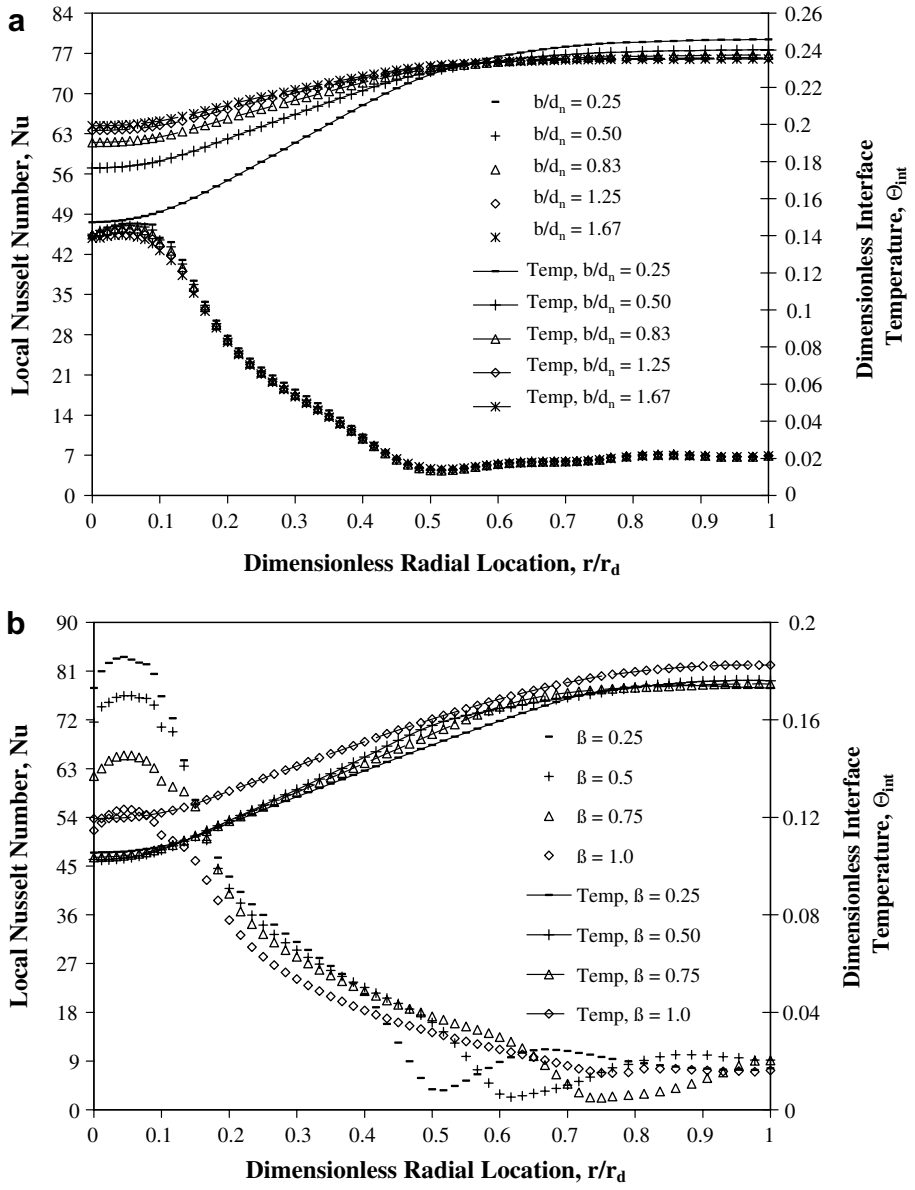

Fig. 6. Local Nusselt number and dimensionless interface temperature distributions for a silicon disk with water as the cooling fluid ($Ek_{1,2} = 4.25 \times 10^{-4}$, $r_p/r_d = 0.667$). (a) Effects of thickness ($Re = 450$, $\beta = 0.5$) and (b) effects of nozzle-to-target spacing ($Re = 900$, $b/d_n = 0.5$).

Therefore, rotational effects cannot propagate very well when the gap between impingement and confinement plates is large. The local maximum is associated with the transition of flow structure from vertical stagnation flow to horizontal boundary layer flow adjacent to the heated disk. The Nusselt number is maximum at the start of the thermal boundary layer. The minimum is associated with the transition from jet momentum dominated flow to rotation dominated flow. As the fluid moves downstream, boundary layer grows in thickness and jet momentum diminishes. On the other hand, the centrifugal force generated by disk rotation increases as the fluid moves to a larger radial location. The balance of these simultaneous effects results in the minimum in local Nusselt number. As both disks are rotating, a smaller vertical gap between disks causes a stronger propagation of rotational effects to the fluid and therefore earlier transition from momentum dominated to rotation dominated flow.

Fig. 7a compares the dimensionless interface temperature results of the present working fluid (water) with three other coolants that have been considered in previous heat transfer studies, namely ammonia (NH_3), flouroinert (FC-77) and oil (MIL-7808) under a Reynolds number of 750. Even though the rotational rate ($\Omega_{1,2}$) for the impinging solid disk and confinement plate was set at 350 rpm the variation of Ekman number occurred since the density (ρ) and dynamic viscosity (μ) are different for each fluid. It may be noticed that MIL-7808 presents the highest dimensionless interface temperature and ammonia has the lowest value. FC-77 shows the most uniform distribution of

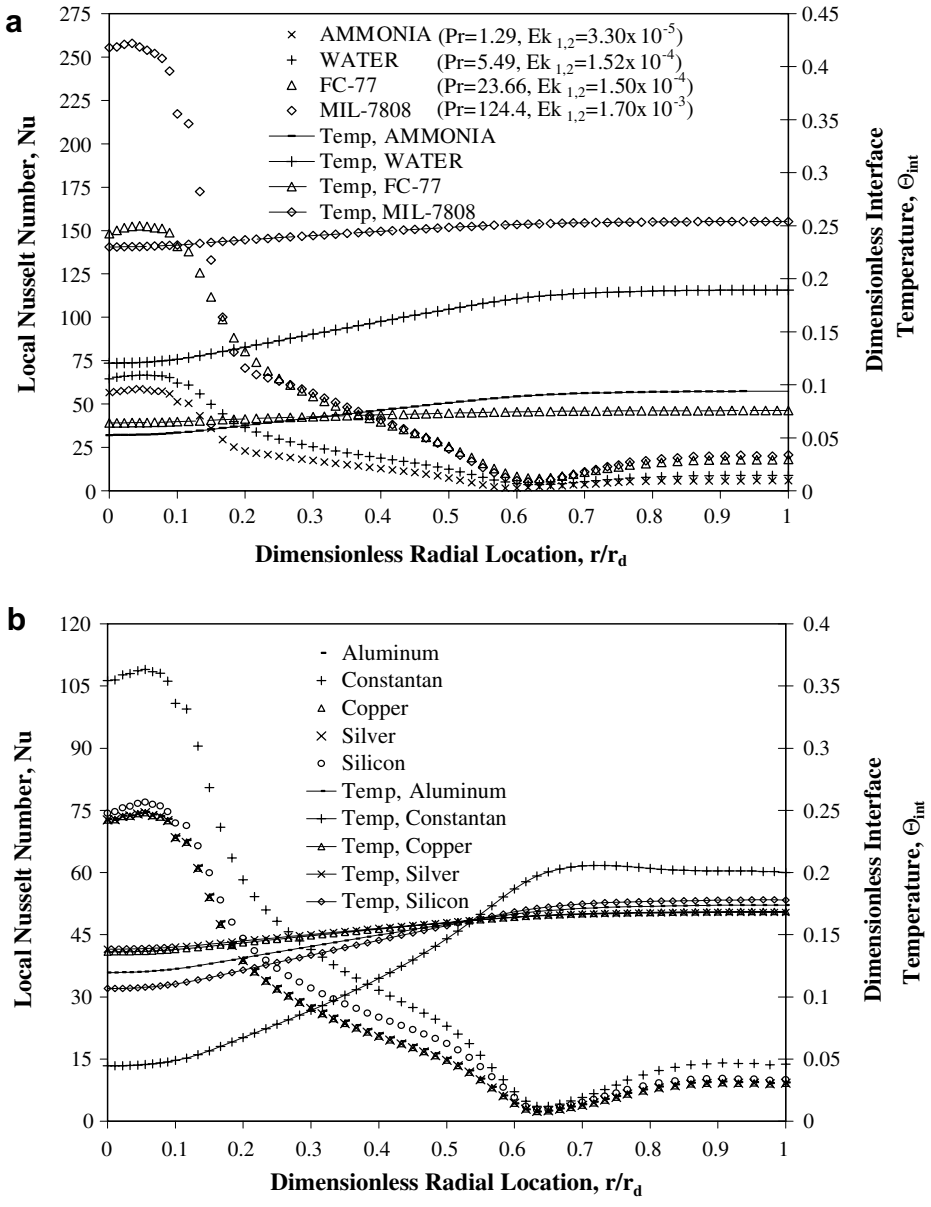

Fig. 7. Effects of fluid and solid properties on local Nusselt number and dimensionless interface temperature ($\beta = 0.5$, $b/d_n = 0.5$, $r_p/r_d = 0.667$). (a) Different cooling fluids with silicon as the disk material ($Re = 750$) and (b) different solid materials with water as the cooling fluid ($Re = 875$, $Ek_{1,2} = 1.77 \times 10^{-4}$).

temperature along the radius of the disk. Fig. 7a shows the corresponding local Nusselt number distributions. It may be noticed that MIL-7808 presents the highest local Nusselt number values over the entire dimensionless radial distance. Ammonia on the other hand provides the lowest Nusselt number. The Nusselt number trend is well correlated with the variation of Prandtl number. A higher Prandtl number fluid leads to a thinner thermal boundary layer and therefore more effective heat removal rate at the interface. The present working fluid results are in agreement with Li et al. [16] and Ma et al. [45] findings where a larger Prandtl number corresponded to a higher recovery factor.

Fig. 7b shows the dimensionless interface temperature and local Nusselt number distribution plots as a function of dimensionless radial distance (r/r_d) measured from the axisymmetric impingement axis for different solid materials with water as the working fluid. The studied materials were aluminum, Constantan, copper, silicon, and silver having different thermo-physical properties. The dimensionless temperature distribution plots reveal how the thermal conductivity affects the heat flux distribution. Constantan shows the lowest temperature at the impingement zone or stagnation point and the highest dimensionless temperature at the outlet in comparison with other solid materials. Copper and silver show a more uniform distribution and higher temperature values at the impingement zone due to their higher thermal conductivity. The dimensionless temperature and local Nusselt number distributions of these two materials are almost identical

due to their similar thermal conductivity values. The crossover of curves for all five materials occurred around $r/r_d \approx 0.525$. This crossover is expected because of thermal energy balance for constant fluid flow and heat input rates. A solid material with a lower thermal conductivity (Constantan) shows a higher maximum local Nusselt number. For all solid materials, the local Nusselt number distribution increases rapidly over a small distance (core region) measured from the stagnation point, reaches a maximum around $r/r_d = 0.05$, and then decreases along the radial distance up to $r_p/r_d \approx 0.63$. Further downstream when the film encounters a free surface at the top along with the rotation of the solid disk at the bottom, the local Nusselt values for all materials gradually increase due to the increment of the tangential velocity and thinner thermal boundary layer that enhances the heat transfer on the solid disk surface.

Six different plate to disk confinement ratios (r_p/r_d) from 0.2 to 0.75 were modeled using water as the coolant and silicon as the disk material. The effects of plate to disk confinement ratio on the dimensionless interface temperature and local Nusselt number at a spinning rate of 125 rpm or $Ek_{1,2} = 4.25 \times 10^{-4}$ and Reynolds number of 450 are shown in Fig. 8. The plots in Fig. 8 reveal that the dimensionless interface temperature increases with the increment of the plate to disk confinement ratio (r_p/r_d). This increment coincides with the increment of liquid film thickness in the free jet region seen in Fig. 3. A thinner film thickness for the same flow rate results in higher fluid velocity near the solid–fluid interface resulting in a higher rate of convective heat transfer. This is seen in the distribution of local Nusselt number plotted in Fig. 8. The local Nusselt number increases with the decrease of plate to disk confinement ratio.

A correlation for the average Nusselt number was developed as a function of confinement ratio, thermal conductivity ratio, dimensionless nozzle-to-target spacing, Ekman number, Reynolds number, and confinement plate to disk radius ratio to accommodate most of the transport characteristics of a semi-confined liquid jet impingement cooling process. The correlation that best fitted the numerical data can be placed in the following form:

$$Nu_{av} = 1.94282 \cdot \beta^{0.111} \cdot Re^{0.75} \cdot Ek_1^{-0.0465} Ek_2^{-0.047} \cdot \varepsilon^{-0.69} \cdot (r_p/r_d)^{-0.05} \quad (20)$$

In developing this correlation, all average Nusselt number data corresponding to the variation of different parameters were used. Only data points corresponding to water as the fluid were used because the number of average heat transfer data for other fluids were small. Also data points corresponding to both disks rotating at the same rate were used. Fig. 9 gives the comparison between the numerical average Nusselt numbers to average Nusselt numbers predicted by Eq. (20). The predicted average Nusselt number values from Eq. (20) deviates in a range of −14.76% to +13.08% from the actual numerical results obtained in present study. The mean deviation is 6.37%. The ranges of the dimensionless variables in this study are the following: $360 \leqslant Re \leqslant 900$, $4.25 \times 10^{-4} \leqslant Ek_1 \leqslant 7.08 \times 10^{-5}$, $4.25 \times 10^{-4} \leqslant Ek_2 \leqslant 7.08 \times 10^{-5}$, $0.25 \leqslant \beta \leqslant 1$, $0.2 \leqslant r_p/r_d \leqslant 0.75$, $Pr = 5.49$, $227.6 \leqslant \varepsilon \leqslant 627.6$. It should be noted from Fig. 9 that a large number of data points are very well correlated with Eq. (20). This correlation can be a convenient tool for the prediction of average heat transfer coefficient.

Fig. 10 shows a comparison of local Nusselt numbers obtained in present numerical simulation with the experimental data obtained by Ozar et al. [34] and numerical

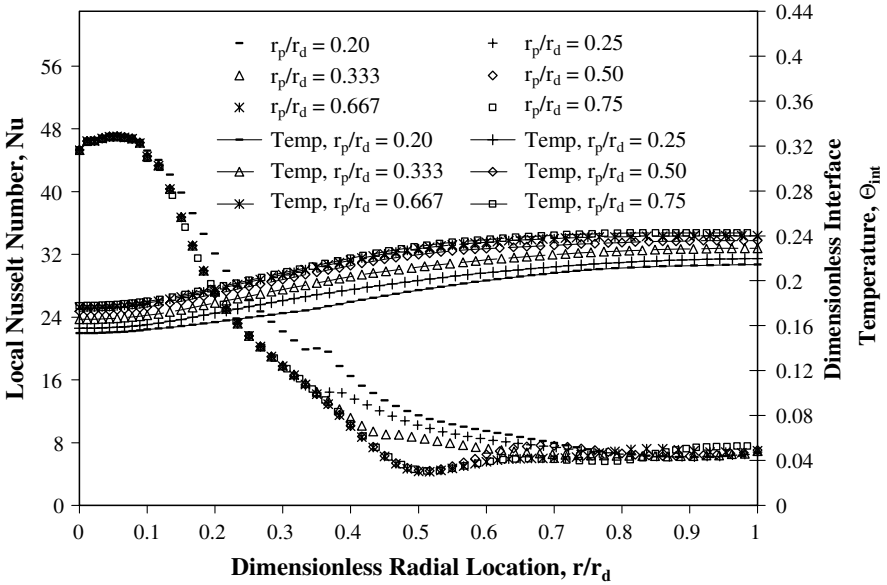

Fig. 8. Local Nusselt number and dimensionless interface temperature distributions for different plate to disk confinement ratio ($Re = 450$, $Ek_{1,2} = 4.25 \times 10^{-4}$, $\beta = 0.5$, $b/d_n = 0.5$).

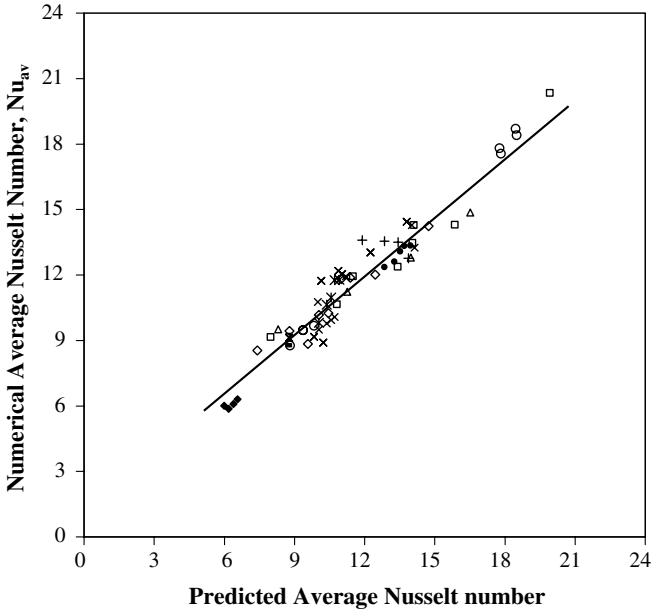

Fig. 9. Comparison of predicted average Nusselt number (Eq. (20)) with numerical data.

results of Rice et al. [35] at various rotational speeds. A rotating disk with a heat flux of 32 kW/m^2, cooled by a round single water jet impingement at a flow rate of 3 l/min ($Re = 238$) and spinning at speeds of 50, 100, 200 rpm were compared. The computation was conducted for jet temperature (T_J) of 293 K; the nozzle-to-target spacing was set to 0.00254 m, with a nozzle diameter of 0.0508 m and for collar (or confinement) that extended over a radial distance of 0.051 m. The spinning disk had a diameter of 0.4064 m and thickness of 0.00635 m. The disk was made of aluminum, a material with a thermal conductivity of 202.4 W/m K. As seen in Fig. 10, the agreement of the local Nusselt number results of Ozar et al. [34] and Rice et al. [35] with the present numerical simulation is satisfactory. The difference in local Nusselt number between Ozar et al. [34] and the present simulation is in the range of 0.79–22.07% with an average difference of 12.33%. The difference in local Nusselt number between Rice et al. [35] and the present simulation falls in the range of 5.01–22.08% with an average difference of 14.9%. The Nusselt number at the stagnation region was compared with the stagnation Nusselt number correlation developed by Liu et al. [46] for liquid jet impingement over a stationary disk. For the Reynolds number and rotational rates considered in this paper, the average difference was 4.22%. The rotation always enhanced the stagnation Nusselt number compared to the stationary disk.

5. Conclusions

The following conclusions could be made based on the numerical results of the present investigation.

1. The increment of Reynolds number contributes to a more effective cooling by increasing the local heat transfer coefficient over the entire solid–fluid interface.
2. For $Ek_{1,2} > 7.08 \times 10^{-5}$, a higher rotational speed enhances the local Nusselt number and generates lower temperature over the entire solid–fluid interface.
3. A higher disk thickness provides more uniform interface temperature and heat transfer coefficient.
4. Heat transfer coefficient increases as the nozzle-to-target distance decreases from $\beta = 1.0$ to 0.2.
5. A reduction in plate to disk confinement ratio increases the local Nusselt number at all locations.
6. A higher Prandtl number fluid leads to a thinner thermal boundary layer and provides a more effective heat removal rate at the solid–fluid interface.

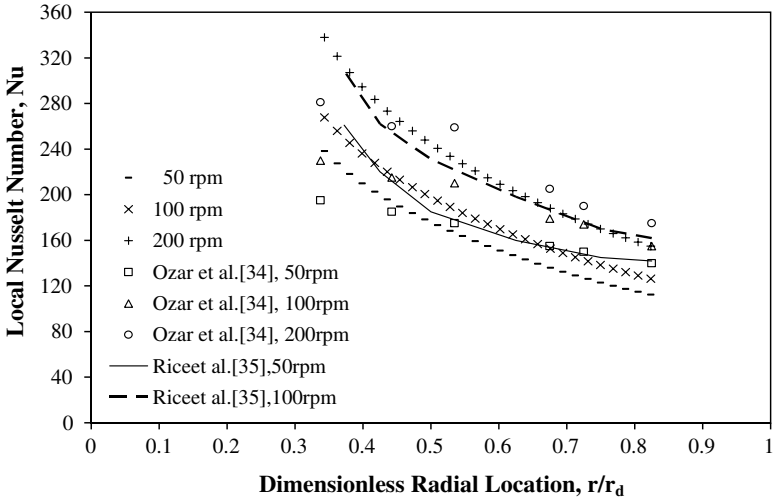

Fig. 10. Comparison of numerical and experimental local Nusselt number distributions at different spinning rates for an aluminum disk with water as the cooling fluid ($T_J = 293$ K, $Re = 238$, $H_n = 0.000254$ m, $b = 0.00635$ m, $b/d_n = 0.125$, $r_p = 0.0508$ m, $r_p/r_d = 0.25$).

7. Plate materials with higher thermal conductivity maintain lower thermal resistance within the solid and therefore a more uniform temperature distribution is achieved at the solid–fluid interface.
8. A correlation for average Nusselt number is proposed in terms of Reynolds number, Ekman numbers (Ek_1, Ek_2), nozzle-to-target spacing ratio, thermal conductivity ratio and confinement plate to disk radius ratio. The differences between numerical and predicted values are in the range of −14.76% to +13.08%. The mean deviation is 6.37%.
9. The numerical results compared reasonably well with available experimental measurements.

References

[1] S. Polat, B. Huang, A.S. Mujumdar, W.J.M. Douglas, Numerical flow and heat transfer under impinging jets: a review, Ann. Rev. Numer. Fluid Mech. Heat Transfer 2 (2) (1989) 157–197.

[2] E.J. Watson, The radial spread of a liquid jet over a horizontal plane, J. Fluid Mech. 20 (3) (1964) 481–499.

[3] Z.H. Chaudhury, Heat transfer in a radial liquid jet, J. Fluid Mech. 20 (3) (1964) 501–511.

[4] M. Korger, F. Krizek, Mass transfer coefficient in impingement flow from slotted nozzles, Int. J. Heat Mass Transfer 9 (1966) 337–344.

[5] M. Kumada, I. Mabuchi, Studies on the heat transfer of impinging jets, Bull. JSME 13 (55) (1970) 77–85.

[6] H. Miyazaki, E. Silberman, Flow and heat transfer on a flat plate normal to a two-dimensional laminar jet issuing from a nozzle of finite height, Int. J. Heat Mass Transfer 15 (1972) 2097–2107.

[7] E.M. Sparrow, T.C. Wong, Impingement transfer coefficients due to initially laminar slot jets, Int. J. Heat Mass Transfer 18 (1975) 597–605.

[8] S. Polat, A.S. Mujumdar, W.J.M. Douglas, Impingement heat transfer under a confined slot jet. Part 1: Effect of surface through flow, Can. J. Chem. Eng. 69 (1991) 266–273.

[9] S. Polat, A.S. Mujumdar, W.J.M. Douglas, Impingement heat transfer under a confined slot jet. Part 2: Effect of surface motion and through flow, Can. J. Chem. Eng. 69 (1991) 274–280.

[10] S. Al-Sanea, Numerical study of the flow and heat-transfer characteristics of an impinging laminar slot-jet including crossflow effects, Int. J. Heat Mass Transfer 35 (10) (1992) 2501–2513.

[11] O.A. Moreno, R.H. Katyl, J.D. Jones, P.A. Moschak, Mass transfer of an impinging jet confined between parallel plates, Int. J. Res. Develop. 37 (2) (1993) 143–154.

[12] B.W. Webb, C.F. Ma, Single-phase liquid jet impingement heat transfer, Adv. Heat Transfer 26 (1) (1995) 105–117.

[13] G.K. Morris, S.V. Garimella, Orifice and impingement flow fields in confined jet impingement, J. Electr. Packag. 120 (1) (1998) 68–72.

[14] S.V. Garimella, B. Nenaydykh, Nozzle-geometry effects in liquid jet impingement heat transfer, Int. J. Heat Mass Transfer 39 (14) (1996) 2915–2923.

[15] J.A. Fitzgerald, S.V. Garimella, A study of the flow field of a confined and submerged impinging jet, Int. J. Heat Mass Transfer 41 (8–9) (1998) 1025–1034.

[16] D.Y. Li, Z.Y. Guo, C.F. Ma, Relationship between the recovery factor and the viscous dissipation in a confined impinging circular jet of high – Prandtl number liquid, Int. J. Heat Fluid Flow 18 (6) (1997) 585–590.

[17] M.M. Rahman, P. Dontaraju, R. Ponnappan, Confined jet impingement thermal management using liquid ammonia as the working fluid, in: Proceedings of the ASME International Mechanical Engineering Congress and Exposition, New Orleans, Louisiana, 2002, pp. 1–10.

[18] C.Y. Li, S.V. Garimella, Prandtl number effects and generalized correlations for confined and submerged jet impingement, Int. J. Heat Mass Transfer 44 (18) (2001) 3471–3480.

[19] A. Chatterjee, L.J. Deviprasath, Heat transfer in confined laminar axisymmetric impinging jets at small nozzle–plate distances: The role of upstream vorticity diffusion, Numer. Heat Transfer Part A 39 (8) (2001) 777–800.

[20] K. Ichimiya, Y. Yamada, Three-dimensional heat transfer of a confined circular impinging jet with buoyancy effects, J. Heat Transfer 125 (2) (2003) 250–256.

[21] Y.L. Shi, M.B. Ray, A.S. Mujumdar, Effects of Prandtl number on impinging jet heat transfer under a semi-confined laminar slot jet, Int. Commun. Heat Mass Transfer 30 (4) (2003) 455–464.

[22] C. Qing-Guang, X. Zhong, W. Yu-Lin, Z. Yong-Jian, Numerical simulation of laminar square impinging jet flows, J. Hydrodyn. Series B 17 (3) (2005) 269–274.

[23] B. Dano, J.A. Liburdy, K. Kanokjaruvijit, Flow characteristics and heat transfer performances of a semi-confined impinging array of jets: effect of nozzle geometry, Int. J. Heat Mass Transfer 48 (3–4) (2005) 691–701.

[24] H.J. Carper Jr., D.M. Deffenbaugh, Heat transfer from a rotating disk with liquid jet impingement, Proceedings of the Sixth International Heat Transfer Conference, Toronto, Canada, vol. 4, Hemisphere Public Corporation, Washington, DC, 1978, pp. 113–118.

[25] H.J. Carper Jr., J.J. Saavedra, T. Suwanprateep, Liquid jet impingement cooling of a rotating disk, J. Heat Transfer 108 (3) (1986) 540–546.

[26] S. Thomas, W.L. Hankey, A. Faghri, T. Swanson, One-dimensional analysis of the hydrodynamics and thermal characteristics of thin film flows including the hydraulic jump and rotation, J. Heat Transfer 112 (3) (1990) 728–735.

[27] S. Thomas, A. Faghri, W.L. Hankey, Experimental analysis and flow visualization of a thin liquid film on a stationary and rotating disk, J. Fluids Eng. 113 (1) (1991) 73–80.

[28] M.M. Rahman, A. Faghri, Numerical simulation of fluid flow and heat transfer in a thin liquid film over a rotating disk, Int. J. Heat Mass Transfer 35 (6) (1992) 1441–1453.

[29] M.M. Rahman, A. Faghri, Analysis of heating and evaporation from a liquid film adjacent to a horizontal rotating disk, Int. J. Heat Mass Transfer 35 (10) (1992) 2655–2664.

[30] A. Faghri, S. Thomas, M.M. Rahman, Conjugate heat transfer from a heated disk to a thin liquid film formed by a controlled impinging jet, J. Heat Transfer 115 (1) (1993) 115–123.

[31] N. Saniei, X. Yan, W. Schooley, Local heat transfer characteristics of a rotating disk under jet impingement cooling, Proceedings of the 11th International Heat Transfer Conference, vol. 5, Kyongju, Korea, 1998, pp. 445–450.

[32] N. Saniei, X. Yan, Experimental study of heat transfer from a disk rotating in an infinite environment including heat transfer enhancement by jet Impingement cooling, J. Enhanced Heat Transfer 7 (4) (2000) 231–245.

[33] B. Ozar, B.M. Cetegen, A. Faghri, Experiments on the flow of a thin liquid film over a horizontal stationary and rotating disk surface, Exp. Fluids 34 (5) (2003) 556–565.

[34] B. Ozar, B.M. Cetegen, A. Faghri, Experiments on heat transfer in a thin liquid film flowing over a rotating disk, J. Heat Transfer 126 (2) (2004) 184–192.

[35] J. Rice, A. Faghri, B.M. Cetegen, Analysis of a free surface film from a controlled liquid impinging jet over a rotating disk including conjugate effects, with and without evaporation, Int. J. Heat Mass Transfer 48 (25–26) (2005) 5192–5204.

[36] L.C. Burmeister, Convective Heat Transfer, second ed., John Wiley and Sons Inc., New York, 1993 (Appendix C pp. 581–590).

[37] C.O. Popiel, L. Boguslawski, Local heat transfer from a rotating disk in an impinging round jet, J. Heat Transfer 108 (2) (1986) 357–364.

[38] J.P. Vanyo, Rotating Fluids in Engineering and Science, Butterworth-Heinemann, Massachusetts, 1993 (Chap. 14, pp. 233–264).

[39] M.N. Özisik, Heat Conduction, second ed., John Wiley and Sons, New York, 1993 (Appendix 1, pp. 657–660).

[40] A. Bejan, Convection Heat Transfer, John Wiley and Sons, New York, 1995 (Appendix C, pp. 595–602).
[41] A.J. Bula, Numerical Modeling of Conjugate Heat Transfer during Free Liquid Jet Impingement, Ph.D. Thesis, University of South Florida, Tampa, FL, 1999.
[42] C.A.J. Fletcher, Computational Galerkin Methods, Springer Verlag, New York, 1984 (pp. 27 and 205).
[43] S. Brodersen, D.E. Metzger, H.J.S. Fernando, Flows generated by the impingement of a jet on a rotating surface, Part 1: Basic flow patterns, J. Fluids Eng. 118 (1) (1996) 61–67.
[44] H. Lachefski, T. Cziesla, G. Biswas, K. Mitra, Numerical investigation of heat transfer by rows of rectangular impinging jets, Numer. Heat Transfer Part A 30 (1) (1996) 87–101.
[45] C.F. Ma, Q. Zheng, S.C. Lee, T. Gomi, Impingement heat transfer and recovery effect with submerged jets of large Prandtl number liquid 2. Initially laminar confined slot jets, Int. J. Heat Mass Transfer 40 (6) (1996) 1491–1500.
[46] X. Liu, J.H. Lienhard, J.S. Lombara, Convective heat transfer by impingement of circular liquid jets, J. Heat Transfer 13 (3) (1991) 571–582.